www.acsnano.org

Exploiting Cation Intercalating Chemistry to Catalyze Conversion-Type Reactions in Batteries

Weiyuan Huang,[#] Jimin Qiu,[#] Yuchen Ji,[#] Wenguang Zhao, Zihang Dong, Kai Yang, Ming Yang, Qindong Chen, Mingjian Zhang, Cong Lin, Kang Xu, Luyi Yang,* and Feng Pan*



Downloaded via UNIV TOWN OF SHENZHEN on November 24, 2025 at 02:03:17 (UTC). See https://pubs.acs.org/sharingguidelines for options on how to legitimately share published articles.

Cite This: ACS Nano 2023, 17, 5570-5578



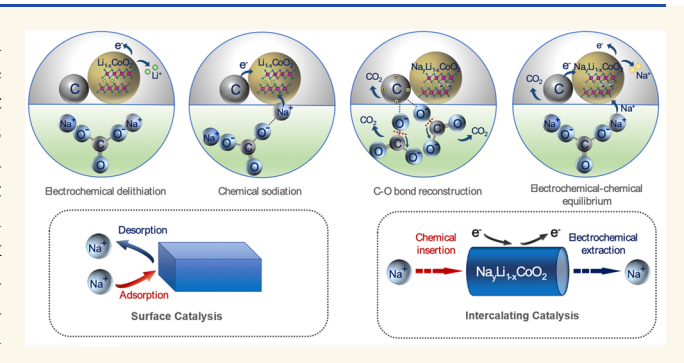
ACCESS I

Metrics & More

Article Recommendations

s Supporting Information

ABSTRACT: Effective harvest of electrochemical energy from insulating compounds serves as the key to unlocking the potential capacity from many materials that otherwise could not be exploited for energy storage. Herein, an effective strategy is proposed by employing LiCoO₂, a widely commercialized positive electrode material in Li-ion batteries, as an efficient redox mediator to catalyze the decomposition of Na₂CO₃ via an intercalating mechanism. Differing from traditional redox mediation processes where reactions occur on the limited surface sites of catalysts, the electrochemically delithiated Li_{1-x}CoO₂ forms Na₂Li_{1-x}CoO₂ crystals, which act as a cation intercalating catalyzer that directs Na⁺ insertion—extraction and



activates the reaction of Na₂CO₃ with carbon. Through altering the route of the mass transport process, such redox centers are delocalized throughout the bulk of LiCoO₂, which ensures maximum active reaction sites. The decomposition of Na₂CO₃ thus accelerated significantly reduces the charging overpotential in Na-CO₂ batteries; meanwhile, Na compensation can also be achieved for various Na-deficient cathode materials. Such a surface-induced catalyzing mechanism for conversion-type reactions, realized *via* cation intercalation chemistry, expands the boundary for material discovery and makes those conventionally unfeasible a rich source to explore for efficient utilization of chemical energy.

KEYWORDS: Na-ion battery, Na-CO₂ battery, catalysis, layered oxide, intercalating redox mediator, cation intercalating chemistry

atalysis pursues more efficient pathways in achieving chemical/electrochemical reactions and has been an indispensable component in various fields including chemical production, pharmaceuticals, and waste disposal. 1-In catalyzing electrochemical processes, redox mediators often serve as the intermediate charge carriers to reduce the kinetic energy barriers leading to final products.^{4,5} In energy storage systems, redox mediators assist charge transfer in those battery materials with poor conductivities or intercept charges and subsequently shuttle them to the counter electrode in order to prevent overcharge.⁶⁻⁸ In recent years, owing to the increasingly approached energy limits imposed by intercalation electrode materials, conversion-type cathode materials with high energy densities are deemed as promising candidates for next-generation batteries, as represented by metal-O₂, metal-S, metal fluorides, and metal-CO₂ batteries. 9-13 However, the insulating nature of the reactants and products often makes their potential capacity inaccessible with high energy barriers, as reflected by extremely high overpotential and poor reversibility and rate capability. Therefore, development of new redox mediators that catalyze both anodic and cathodic reactions and understanding their working mechanism have become a highly urgent direction. ^{6–8,16}

In general, catalysis reactions assisted by redox mediators take effect at either solid—gas, solid—liquid, or solid—solid interfaces; hence, their efficiency is highly dependent on the interfacial active sites, ¹⁷ while their bulk are inaccessible to the reactants and remain inactive. One way to resolve this issue is *via* single-site catalysts, which could maximize the surface-to-volume ratio ^{18,19} but require a complicated synthesis process. To this date, how to activate the bulk phases of mediators and make them available for charge mediation remains a challenge.

Received: November 5, 2022 Accepted: March 2, 2023 Published: March 9, 2023





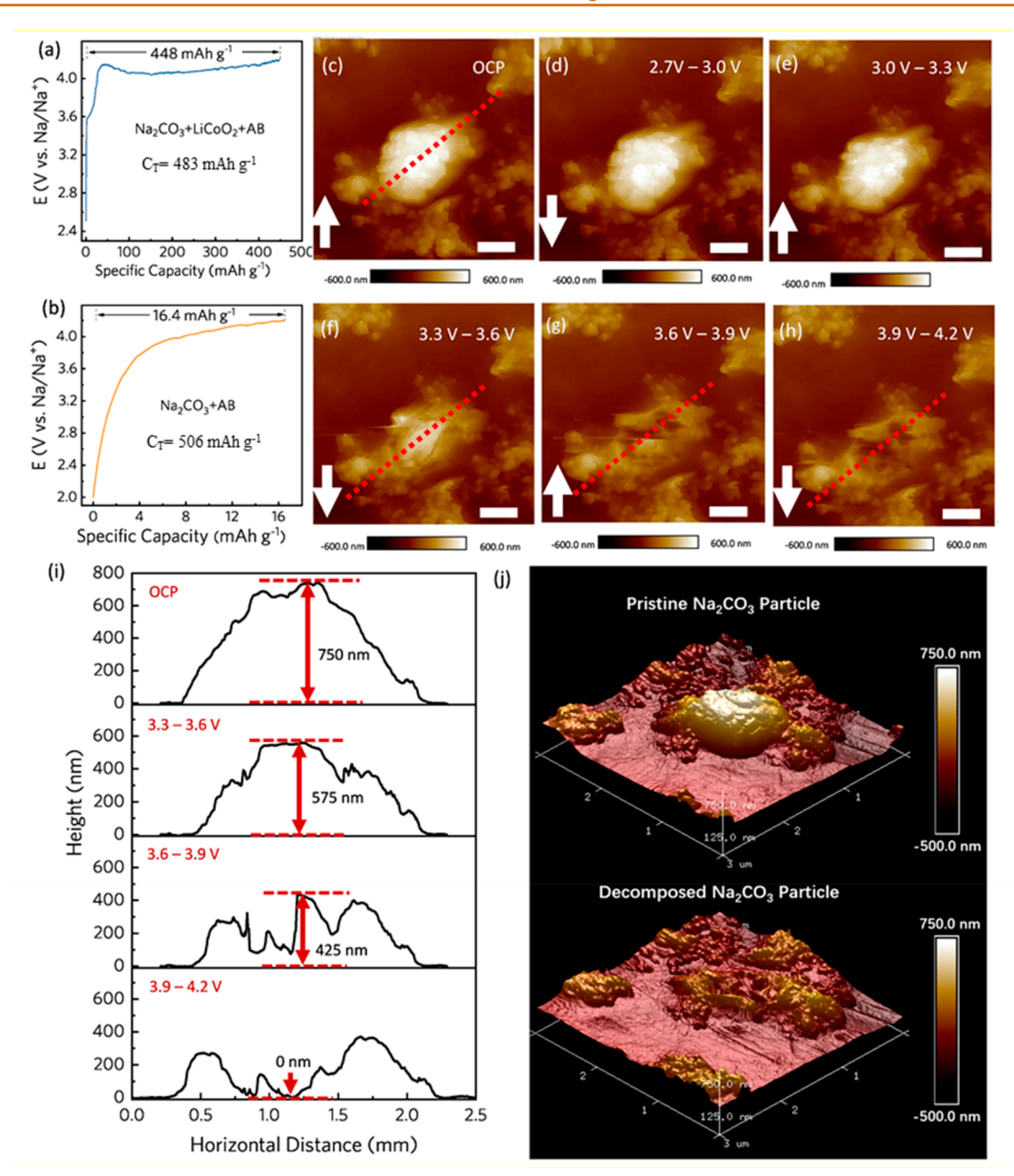


Figure 1. Electrochemical oxidation and morphology evolution of Na_2CO_3 . First-cycle voltage profiles of (a) SC-LCO and (b) neat Na_2CO_3 , respectively (cutoff voltage, 4.2 V vs Na/Na^+ ; specific current, 10 mA g^{-1}). Images of a spot taken at various voltages: OCP (c), from 2.7 to 3.0 V (d), from 3.0 to 3.3 V (e), from 3.3 to 3.6 V (f), from 3.6 to 3.9 V (g), and from 3.9 to 4.2 V (h) (scale bar = 500 nm). (i) Quantitative measurements of the Na_2CO_3 particle height variation at different voltages. (j) 3D simulation images of the electrode surface at OCP and 4.2 V.

In addition to the limited active sites on the surface, the rate of catalytic reaction is also largely determined by the mass transport process toward or away from the interfaces, which further places limitations on reaction efficiency and rate *via* diffusion coefficient and concentration of the reactant.³

As a nontraditional electrode material, Na₂CO₃ exhibits an extremely high specific capacity (over 500 mAh g⁻¹) and low costs. The capability of decomposing Na₂CO₃ electrochemically would create benefits in both Na-CO₂ batteries and Na compensation in sodium-ion batteries. However, Na₂CO₃ is an electronic as well as ionic insulator, which prohibits the access to its promising capacity; therefore no one has seriously considered such a possibility. Previously, transition metal oxides have been shown to promote LiF splitting *via* surface-

induced conversion reactions.^{20,21} In this work, we broke through the above limitations and employed LiCoO₂ (LCO), a commercially used cathode material for Li-ion batteries, as a redox-mediating catalyst, which effectively harnesses the electrochemical energy contained within Na₂CO₃, and achieved a specific capacity of 448 mAh g⁻¹. Assisted by various *in situ* and *ex situ* characterization techniques, we revealed that, instead of following the traditional adsorption—desorption catalyzing processes at the interface, electrochemically delithiated Li_{1-x}CoO₂ serves as an intercalating redox mediator that extracts Na⁺ from Na₂CO₃ into its bulk phase, forming Na_yLi_{1-x}CoO₂, which will be subsequently oxidized again. The kinetics of the altered reaction pathway are significantly boosted because of the participation of the active

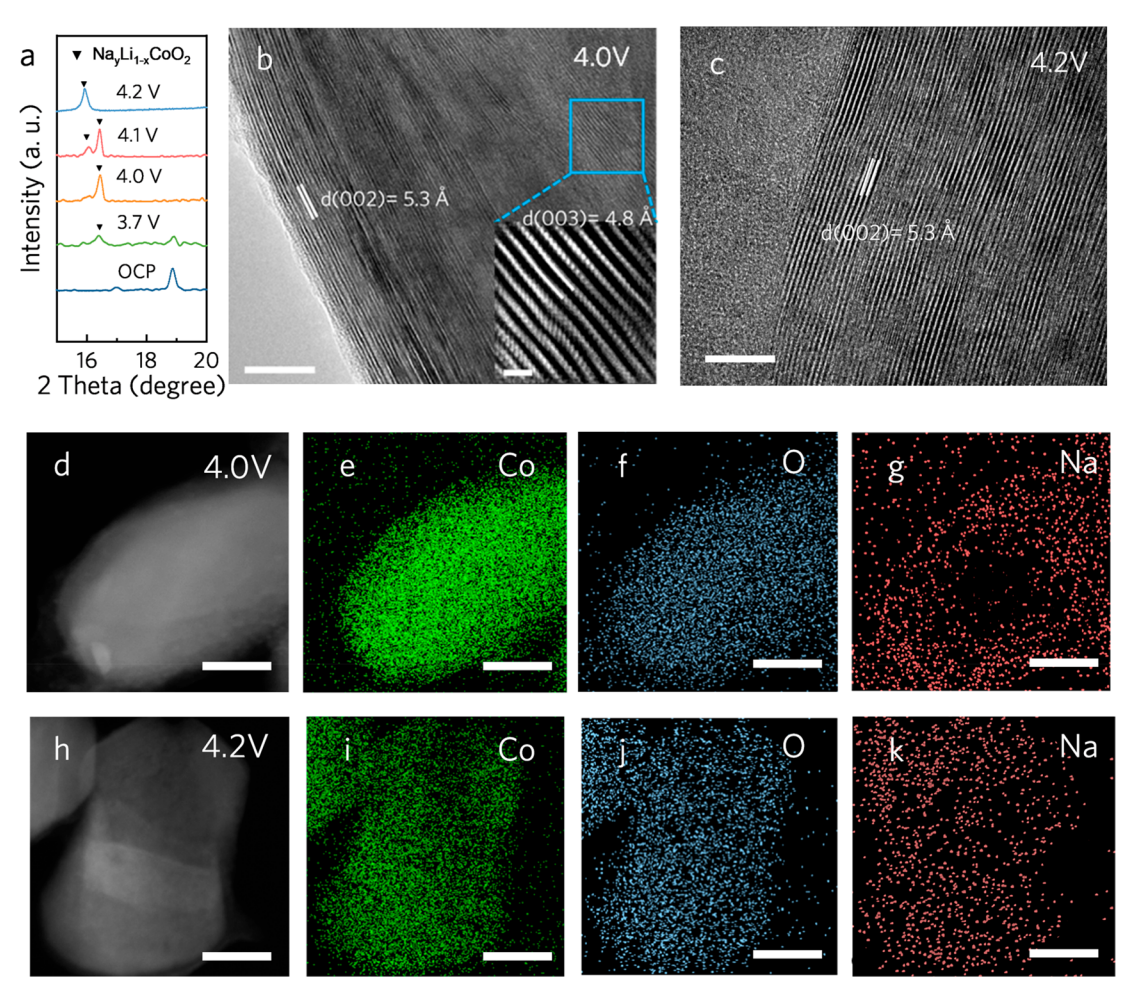


Figure 2. Na⁺ intercalation into LCO. (a) Ex situ XRD patterns SC-LCO electrode at different charge states. (b) TEM images of LCO particles charged to 4.0 V vs Na/Na⁺ in the presence of Na₂CO₃ (scale bar = 10 nm). The interlayer spacings of the exterior and interior (inset, scale bar = 1 nm) are measured, respectively. (c) TEM images of Na particles charged to 4.2 V vs Na/Na⁺ in the presence of Na₂CO₃ (scale bar = 10 nm). TEM image and the corresponding EDS of LCO particles when charged to (d-g) 4.0 V and (h-k) 4.2 V.

sites in the bulk $Na_yLi_{1-x}CoO_2$, which effectively activates the Na_2CO_3 for electrochemical oxidation. Moreover, highly efficient Na compensation can also be achieved for Na-deficient cathode materials. The discovery of the intercalation-based catalysis chemistry not only contributes to the practical application of conversion-type electrode material but also provides accesses to many more materials that have once been thought impossible for electrochemical reactions.

RESULTS AND DISCUSSION

Boosting Effect on Na₂CO₃ Decomposition. Na₂CO₃ (SC) powders were first ball-milled for 20 h to reduce particle size to $1-3~\mu m$ (Supporting Information (SI) Figure S1). The Bragg diffraction peaks fit well with the typical Na₂CO₃ with a C2/m space group in the absence of obvious impurity (SI Figure S2a). LCO particles with size around 100–300 nm (SI Figure S3) was synthesized via a sol–gel process, whose X-ray diffraction (XRD) pattern (SI Figure S2b) is in good agreement with the typical LiCoO₂ structure (space group R3m, JCPDF No. 50-0653). The transmission electron microscopy (TEM) image of prepared LCO (SI Figure S4) shows a regular layered structure with layer spacing of ~4.8 Å, consistent with previous reports. Simple ball-milling treatment is carried out to ensure homogeneous mixing between the two components in SC-LCO composite

 $(m_{SC}:m_{LCO} = 9:1)$. The prepared Na₂CO₃ electrodes consist of active materials (Na₂CO₃ or SC-LCO composite), acetylene black (AB) and poly(vinylidene fluoride) (PVDF) binder in the mass ratio of 8:1:1. The galvanostatic oxidation curves (Figure 1a,b) demonstrate that, compared with the neat Na₂CO₃ electrode, which can only deliver a limited specific capacity of 16.4 mAh g⁻¹, the SC-LCO electrode exhibits a dramatically improved charge capacity of 448 mAh g⁻¹ (theoretical capacity $C_T = 483$ mAh g⁻¹) under the same cutoff potential (4.2 V vs Na/Na⁺). Electrochemical results obtained under different mass ratios and current densities are demonstrated in SI Figure S5. These results indicate that LCO must have cast a significant influence over the electrochemical decomposition reaction of Na₂CO₃. The evident change of the electrode morphology (SI Figures S6 and S7a,b) as well as the disappearance of Na in the corresponding elemental distributions (SI Figure S7c,d) at 4.2 V vs Na/Na+ clearly revealed the desodiation of Na₂CO₃ and its conversion. Interestingly, differing from SI Figure S6c, where the elemental distributions of Na and Co are separated, corresponding to SC and LCO, respectively, the distributions of Na and Co in SI Figure S5d are overlapped as demonstrated by the highlighted spots. Therefore, it can be speculated that a compound containing Na and Co was formed during the oxidation process.

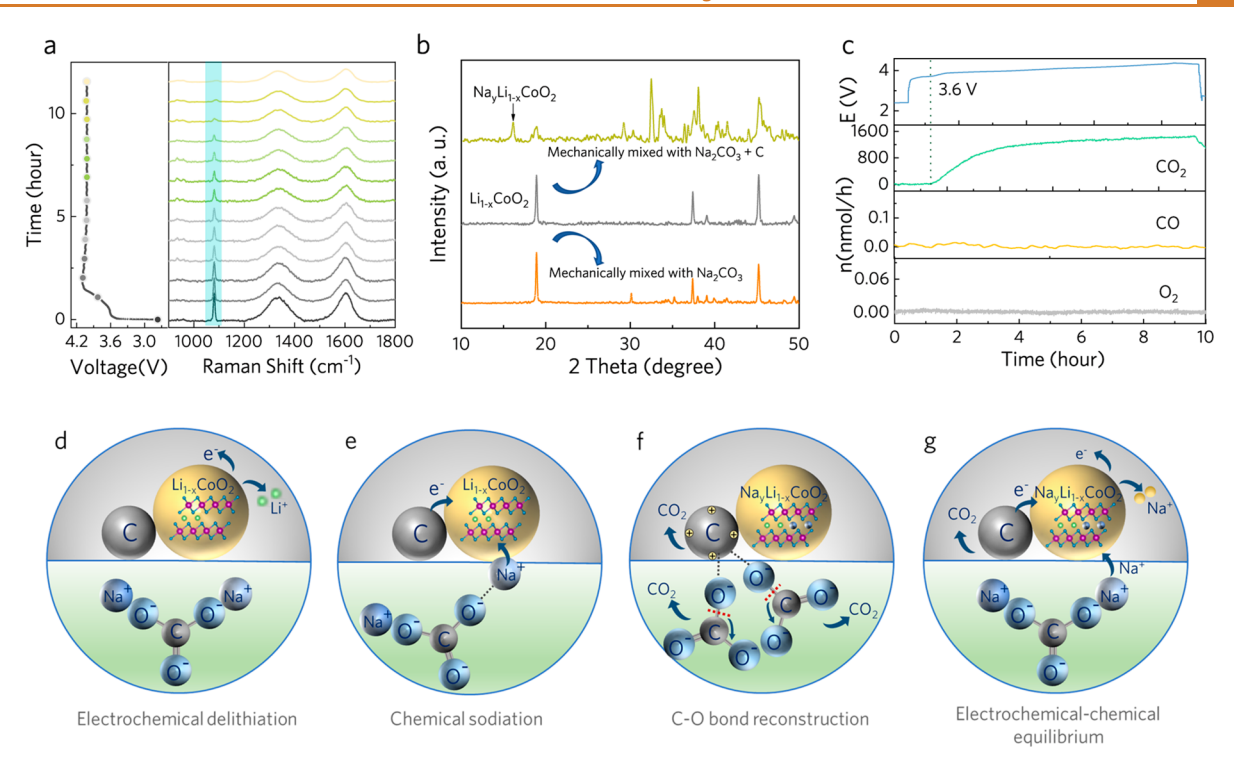


Figure 3. Exploration of reaction mechanism. (a) Galvanostatic charge curve and corresponding in situ Raman spectra of the SC-LCO composite. (b) XRD patterns of $\text{Li}_{1-x}\text{CoO}_2$ and its mixture with Na_2CO_3 and Na_2CO_3 + C after mixing and grinding. (c) DEMS tests presenting the galvanostatic charge curve and the detection of gases released synchronously. Proposed reaction mechanism for Na_2CO_3 decomposition and potential applications in Na-ion batteries. (d) Initial oxidation of LCO and the relevant reactions. (e) Proposed Na^+ intercalation into $\text{Li}_{1-x}\text{CoO}_2$ and carbon oxidation. (f) Reconstruction of C-O bonds and the release of CO_2 . (g) Overall reaction mechanism.

In situ atomic force microscopy (AFM) (setup shown in SI Figure S8) was applied to visually observe how Na₂CO₃ decomposes in the presence of LiCoO2, which is driven by the applied potential from the linear sweep voltammetry (SI Figure S9). The corresponding AFM morphology images are simultaneously recorded (Figure 1c-h). A large Na₂CO₃ particle with the size of about 1 μ m can be observed from the AFM image (Figure 2b) at OCP, which is in accordance with the size of Na₂CO₃ (SI Figure S1). Quantitative analysis of the height variation during electrochemical processes also was conducted along the longitudinal section of the red dotted line in the Na₂CO₃ particle (Figure 1i), where the pristine Na₂CO₃ particle is about 750 nm at OCP. Upon charging, the Na₂CO₃ particle remained unchanged between 2.4 and 3.3 V vs Na/Na⁺, indicating the absence of reaction in this potential range. However, at around 3.6 V vs Na/Na⁺, a dramatic change occurs to the particle morphology, with the height decreasing to 575 nm. The reaction continues afterward, until the height of the Na₂CO₃ particle eventually decreased to 0 nm around 4.2 V vs Na/Na⁺. Figure 1j demonstrates the 3D simulation image of Na₂CO₃ particle during this oxidative decomposition. By sharp contrast, in situ AFM results for Na₂CO₃ particles in the absence of LCO experiences negligible morphology change in the same potential range (SI Figure S10), confirming the intrinsic nature of Na₂CO₃ particles in resisting electrochemical reaction.

Spontaneous Na⁺ Intercalation in Bulk LCO. Linear sweep voltammetry results (SI Figure S11) also shows that, in the absence of LCO, the onset voltage where the negligible decomposition of neat Na_2CO_3 occurs is 3.86 V vs Na/Na^+ . In the presence of LCO, this potential is dropped to 3.56 V vs

Na/Na⁺, which agrees well with AFM results and is the well-known delithiation potential of LCO. More importantly, much higher peak current density was observed from the SC-LCO composite, which must be apparently ascribed to a faster kinetics of Na₂CO₃ oxidation. *In situ* electrochemical quartz crystal microbalance (EQCM) was also applied, which measures the mass loss of composite electrode during the charging process (SI Figure S12) and further confirms that the onset decomposition potential for Na₂CO₃ in the presence of LCO is 3.6 V vs Na/Na⁺. Although EQCM failed to yield a quantitative number for the lost species, it is resonable to speculate that the reaction of Na₂CO₃ produces a gaseous or soluble product that leaves the substrate, which is induced by the oxidation (delithiation) of LiCoO₂.

Ex situ XRD was performed to track the component evolution of the electrode upon the charge process. Characteristic diffraction peaks of both Na₂CO₃ and LCO can be found in the XRD patterns (Figure 2a) at OCP. When charged to 3.7 V vs Na/Na $^+$, the new diffraction peaks appeared at $\sim 16^{\circ}$ and \sim 32° can be indexed to the P3-phase Na, CoO₂ structure, ^{27,28} indicating that the delithiated LCO will partially turn into Na_vCoO_2 , forming $Na_vLi_{1-x}CoO_2$. In and ex situ XRD results (SI Figures S13 and S14) also verified the formation of Na_vCoO₂ occurred above 3.66 V vs Na/Na⁺. As the potential increased, the LCO phase gradually turned into Na_vLi_{1-x}CoO₂ and disappeared at 4.2 V. The TEM image (Figure 2b) shows that, at 4.0 V vs Na/Na+, the Na+ insertion process first enlarged the interlayer spacing at the exterior part of LCO particle from 4.8 to 5.3 Å, confirming the formation of Na_vCoO₂ structure, which will continuously propagate to the bulk during the subsequent oxidation process as demonstrated

by the TEM image of LCO particle charged to 4.2 V (Figure 2c). This finding is supported by the energy dispersive spectra (EDS) of LCO particles in the composite charged to different potentials: at 4 V vs Na/Na⁺, Na only exists at the exterior part of the particle, whereas at 4.2 V vs Na/Na⁺, Na distributed homogeneously in the particle. The spreading tendency of Na inwardly in the particle coincides with the propagation of the Na_vLi_{1-x}CoO₂ phase. It should be noted that as the voltage increased from 4.0 to 4.1 V (corresponding to the oxidation plateau shown in Figure 1a), the (002) diffraction peak positions for Na_vLi_{1-x}CoO₂ barely shift, while Na₂CO₃ is being continuously consumed (as shown in the ex situ Fourier transform infrared spectra, SI Figure S15), suggesting a relatively equilibrium state of Na_vLi_{1-x}CoO₂ can be retained for Na₂CO₃ oxidation. When the voltage reached 4.2 V vs Na/ Na⁺, the peaks for Na₂CO₃ disappeared completely, accompanied by a blue shift of (002) peak of Na_vCoO₂ at ~16° (zoomed out part in Figure 2b) as well as the position shift of the Co 2p_{3/2} main peak toward higher binding energy in X-ray photoelectron spectra (XPS) (SI Figure S16). Both changes indicate the electrochemical oxidation of Co nuclei in Na_vLi_{1-x}CoO₂, which occurs because the equilibrium described above is breached by the depletion of Na₂CO₃, leading to the apparent Na⁺ deintercalation from Na_vLi_{1-x}CoO₂. Inductively couple plasma atomic emission spectroscopy (ICP-AES) results (see detailed data in SI Table S1) reveal that the chemical compositions of Na_vLi_{1-x}CoO₂ particle obtained at 4.0 and 4.2 V vs Na/Na⁺ are Na_{0.35}Li_{0.2}CoO₂ and Na_{0.32}Li_{0.12}CoO₂, respectively.

For LCO, electrochemical sodiation represents reduction, which only occurring during discharging; hence, this counterintuitive behavior suggests a hitherto unknown reaction route. To rule out the electrochemical sodiation process, the LiCoO₂llNa half-cells with a sodium-ion electrolyte were assembled and charged to different voltages, whose XRD patterns (SI Figure S17) detect no peak for Na_yCoO₂ even when the cell was charged to 4.2 V vs Na/Na⁺. We speculate that the formation of Na_yCoO₂ can only originate from chemical reactions involving Na₂CO₃.

Redox Mediated Na₂CO₃ Decomposition. According to previous studies, ^{14,29} the electrochemical oxidation of Na₂CO₃ most likely occurs *via* at least one of the following reaction routes:

route 1:

$$2Na_2CO_3 + C - 4e^- \rightarrow 4Na^+ + 3CO_2\uparrow \tag{1}$$

route 2:

$$2Na_2CO_3 - 4e^- \rightarrow 4Na^+ + 2CO_2\uparrow + O_2\uparrow \tag{2}$$

To reveal the detailed reaction mechanism, in situ shell-isolated nanoparticle-enhanced Raman spectroscopy (SHINERS) was employed. As shown in Figure 3a, during the electrochemical oxidation process the peak at $\sim 1080~\rm cm^{-1}$ (corresponding to Na₂CO₃) decreased gradually, which can be assigned to the decomposition reaction of Na₂CO₃. Interestingly, the intensities of both D and G bands of carbon in Figure 3a also attenuated with cycling, suggesting that conductive carbon has participated in the reaction.

To further identify the role of carbon in the reaction, LCO is first charged to 4.0 V vs Na/Na⁺ in the absence of carbon into Li_{1-x}CoO₂. Then the delithated Li_{1-x}CoO₂ is mixed with neat

 Na_2CO_3 and $Na_2CO_3 + C$, which were ground in a mortar, respectively. The XRD patterns of both products (Figure 3b) clearly show that, in the presence of carbon, formation of $Na_yLi_{1-x}CoO_2$ occurred, while no new peaks can be found in the absence of carbon. This result not only further proves that the overall reaction is neither purely chemical nor purely electrochemical but instead electrochemical—chemical coupled, but also reveals the importance of carbon as an electron donor to negate the electronic insulating nature of Na_2CO_3 .

Additionally, since both eq 1 and eq 2 can be easily differentiated by analyzing their gaseous products, we applied in situ differential electrochemical mass spectroscopy (DEMS) to further confirm the reaction mechanism. For SC-LCO (Figure 3c), CO₂ was detected from 3.6 V vs Na/Na⁺ with no sign of O2 during the whole charging process. More importantly, a quantitative analysis is carried out to determine whether the generated CO₂ comes from Na₂CO₃ decomposition (see SI Figure S18 for detailed calculation). According to eq 1, the theoretical amount of CO2 released is calculated to be 5.34×10^{-6} mol based on the accumulative charge transferred between 3.6 and 4.0 V vs Na/Na+, which agrees with the actual amount of CO₂ released, 5.05×10^{-6} mol, that was measured by DEMS, confirming that the product of carbon winds up as CO₂. Therefore, the oxidation mechanism for Na₂CO₃ can be summarized as the chemical reaction between Li_{1-x}CoO₂, Na₂CO₃, and carbon:

$$\operatorname{Li}_{1-x}\operatorname{CoO}_2 + \frac{y}{2}\operatorname{Na}_2\operatorname{CO}_3 + \frac{y}{4}\operatorname{C} \to \operatorname{Na}_y\operatorname{Li}_{1-x}\operatorname{CoO}_2 + \frac{3y}{4}\operatorname{CO}_2\uparrow \tag{3}$$

As no obvious position shift in the Co $2p_{3/2}$ main peak can be observed by *ex situ* XPS spectra from 3.7 to 4.1 V *vs* Na/Na⁺ (SI Figure S14). This could be attributed to a dynamical equilibrium (indicated by the flat charge plateau) between the redox center (Co) and the reactant CO_3^{2-} , where the rate of electrochemical reaction (eq 4) approximately equals that of chemical reaction (eq 5). Hence a steady state has been established between the constant consumption of Na₂CO₃ and electrochemical oxidation of cobalt:

$$Na_yLi_{1-x}CoO_2 - ze^- \rightarrow Na_{y-z}Li_{1-x}CoO_2 + zNa^+$$
 (4)

$$Na_{y-z}Li_{1-x}CoO_2 + \frac{z}{2}Na_2CO_3 + \frac{z}{4}C$$

$$\rightarrow Na_yLi_{1-x}CoO_2 + \frac{3z}{4}CO_2\uparrow$$
(5)

$$2Na_2CO_3 + C - 4e^{-} \xrightarrow{Na_yLi_{1-x}CoO_2} 4Na^{+} + 3CO_2 \uparrow$$
 (6)

It should be noted that the amount of Li⁺ in the Na_yLi_{1-x}CoO₂ was limited compared to Na⁺ available from Na₂CO₃ decomposition (approximately 1:20 in molar ratio). Consequently, the extraction of Li⁺ during the decomposition process could be ignored, and the whole process can be seen as Na₂CO₃ releasing Na⁺ to the electrolyte through Na_yLi_{1-x}CoO₂ in the role of catalyzer, which keeps the same thermodynamic enthalpy in fully chemical reaction without changing its composition (eq 6). As metallic Na is adopted as the counter electrode in this study, the overall reaction could be written as

$$2Na_2CO_3 + C \xrightarrow{Na_yLi_{1-x}CoO_2} 4Na + 3CO_2 \uparrow$$
 (7)

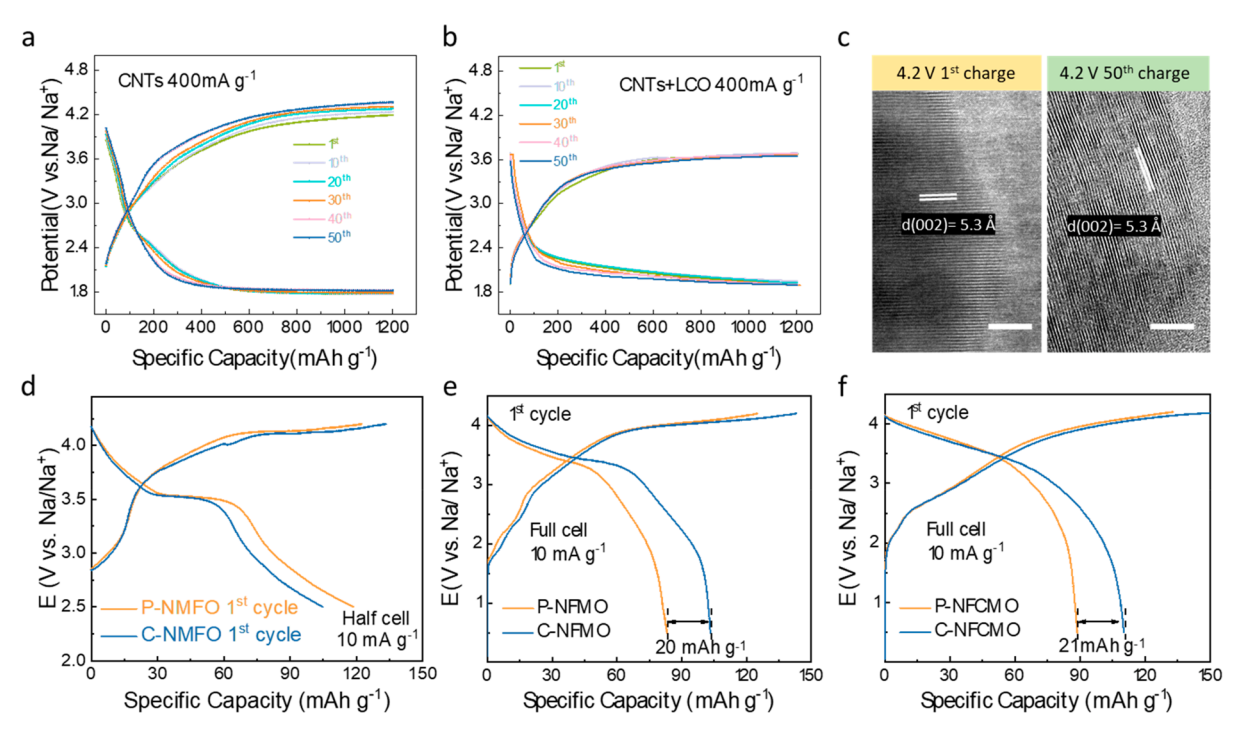


Figure 4. Improved Na-ion battery performance with the help of LCO. Voltage profiles of Na-CO₂ cells with (a) CNTs and (b) CNTs + LCO electrodes under different cycle numbers with a limited specific capacity of 1200 mAh $\rm g^{-1}$, at 400 mA $\rm g^{-1}$. (c) TEM images of Na_yLi_{1-x}CoO₂ particles after first and 50th cycles (scale bar = 10 nm). (d) Initial galvanostatic voltage profiles of C-NMFO and P-NMFO in half-cells at the current density of 10 mA $\rm g^{-1}$. (e) Initial galvanostatic voltage profiles of C-NMFO||hard carbon and P-NMFO||hard carbon full cells at the specific current of 10 mA $\rm g^{-1}$. (f) Initial galvanostatic voltage profiles of C-NFCMO||hard carbon and P-NFCMO||hard carbon full cells at the specific current of 10 mA $\rm g^{-1}$.

From the results demonstrated above, the electrochemicalchemical coupled catalysis mechanism is proposed. Upon charging, LCO undergoes electrochemical delithiation to form Li_{1-x}CoO₂ (Figure 3d). Exhibiting high electrochemical oxidation potential, the metastable Li_{1-x}CoO₂ not only draws Na+ from Na2CO3 into its layered structure by breaking the strong O-Na ionic bond but also extracts electron from the carbon by oxidizing it (Figure 3e). As an extremely strong Lewis acid, the positively charged carbocation simultaneously combines with strong Lewis base (i.e., CO₃²⁻) through C-O bond reconstruction to form CO₂ (Figure 3f). The resulting Na_vLi_{1-x}CoO₂, which plays an intercalation catalyst to extract Na⁺ as driven by electrochemical potential while inserting Na⁺ from Na₂CO₃, will be electrochemically oxidized again and the process is repeated (Figure 3g) until the depletion of Na₂CO₃, which cuts off the reaction loop and leads to net desodiation. The potential difference of particles- or facets-driven spontaneous cation transfer between solid-solid interphases has been previously reported in positive materials for Li-ion batteries.³⁰⁻³² In this case, differing from traditional catalysis following an adsorption-desorption process on an active facet on interfaces, an intercalation-based redox mediator extends the mass transport (i.e., Na⁺) deep into the interior of LCO lattice. Therein, active redox centers (Co) are delocalized, which enables the maximum use of the bulk of catalysts. To confirm this feature, the size effect of LCO particles is also investigated; it is found that by using larger LCO particles (~1 μm), a large decomposition capacity of Na₂CO₃ (278 mAh g⁻¹) can still be achieved (SI Figure S19). Therefore, this type of redox mediator is much less dependent on the surface area compared with traditional ones, demonstrating enormous potential for practical applications. We speculate that Li

(Na)-ion diffusion in $Na_yLi_{1-x}CoO_2$ might be the rate-determining step in larger particles, as it is the case in many intercalating cathode materials. Therefore, in future study, it is worth looking for ion hosts with better charge mobility.

Application in Na-Ion Batteries. To leverage the proposed mechanism in a Na-CO₂ battery, cathodes consisting of carbon nanotubes (CNTs) and LCO are prepared (SEM images are shown in SI Figure S20), while bare CNTs electrodes are used as control. Galvanostatic cycling with fixed discharge/charge capacity of 1200 mAh g-1 is carried out at the specific current of 400 mA g⁻¹. As shown in Figure 4a,b, the much lower charging voltage plateau of CNTs + LCO (~3.65 V) compared with bare CNTs electrode (>4.2 V) indicates that the discharge product can be efficiently oxidized. This result outperforms many nanosized catalysts and is comparable with noble metal-based ones for Na-CO₂ batteries (SI Table S2). The SEM images of CNTs + LCO electrodes after cycling were taken to verify the reversibility of the Na-CO₂ battery. The Na₂CO₃ particles were decomposed at 3.6 V and regenerated when discharged to 1.8 V after first and 10th cycles (SI Figure S21). The CNTs also participated in the decomposition reaction and still existed after cycling (SI Figures S22 and S23). By comparing the TEM images of Na_vLi_{1-x}CoO₂ particles at different cycle numbers, it can be observed that the layered structure of Na_vLi_{1-x}CoO₂ particles is well-preserved after 50 cycles (Figure 4c), which is supported by the XRD results (SI Figure S24). Owing to the excellent structural reversibility, the charging potential of CNTs + LCO electrode remained relatively stable (SI Figure S25). Moreover, the effectiveness of CNTs + LCO in reducing the overpotential is more prominent under a higher specific current of 2000 mA g⁻¹ (SI Figure S26).

Alternatively, the proposed mechanism has also been explored as a Na-compensation method for Na-deficient P2-type Na-ion cathodes. The SC-LCO composite was applied to Na-ion half-cells with Na-deficient P2-type cathodes Na $_{0.7}$ Mn $_{0.6}$ Fe $_{0.4}$ O $_{2}$ (NMFO). At the current density of 10 mA g $^{-1}$, a higher initial specific charge capacity can be achieved in C-NFMO half-cell (Figure 4d). Note that the mass of the SC-LCO composite has been included in the specific capacity calculation for C-NFMO. By contrast, the addition of Na $_{2}$ CO $_{3}$ itself cannot provide extra capacity for NFMO (SI Figure S27). To further evaluate the effect of SC-LCO under more practical situations, hard carbon was chosen as a Na-deficient anode to assemble full cells with an N/P ratio of 0.83 (*i.e.*, cathode-controlled type).

In the presence of SC-LCO, the initial specific discharge capacity is improved by 20 mAh g $^{-1}$ at the current density of 10 mA g $^{-1}$ (Figure 4e), which is in accordance with results of half-cells. This result outperforms currently reported oxide Nacompensation additives (SI Table S3). A similar Nacompensation effect can also be achieved in Na $_{0.7}$ Fe $_{0.4}$ Cu $_{0.1}$ Mn $_{0.5}$ O $_{2}$ (NFCMO)llhard carbon (Figure 4f) and Na $_{0.7}$ Mn $_{0.75}$ Co $_{0.25}$ O $_{2}$ (NCMO)llWSe $_{2}$ full cells (SI Figure S28), demonstrating the high universality of this stragety.

CONCLUSIONS

In this work, we have discovered Na_vLi_{1-x}CoO₂, which is formed from a LiCoO₂ via electrochemical process, as a cation intercalating catalyst to activate the electrochemical oxidation of Na₂CO₃. It is demonstrated that the composite electrode follows an electrochemical-chemical coupled reaction mechanism, where electrochemically delithiated Li_{1-x}CoO₂ serves as an intercalating redox mediator to achieve spontaneous bulk insertion of Na⁺ and oxidation of carbon. Unlike traditional catalyzing reactions that solely rely on single-site adsorptiondesorption processes, the spontaneous cationic intercalation fully uses the bulk of catalysts via delocalizing active redox centers to sync-break ionic bond $(2Na^+-(CO_3)^{2-})$ and covalent bond $(C^{4+}-O^{2-}$ in $(CO_3)^{2-})$. As a result, efficient decomposition of Na₂CO₃ can be attained. The proposed chemistry is furthermore found to not only reduce the charging overpotential in Na-CO₂ batteries but also enable Na compensation for various Na-deficient P2-type cathode materials. We believe that the discovery of the mechanism can enable inexpensive energy storage materials from those compounds that were traditionally thought unfeasible for harnessing electrochemical energy.

EXPERIMENTAL SECTION

Synthesis of LiCoO₂. The LiCoO₂ nanoparticles were synthesized by a sol–gel process. First, $Co(CH_3COO)_2$ · $4H_2O$ and $Li(CH_3COO)_2$ · $2H_2O$ were dissolved in deionized water in a molar ratio of 1:1. Then the critric acid monohydrate and ethelene glycol mixing solution (in a 1:4 molar ratio) was slowly dropped into the above solution. The resulting solution was stirred at 90 °C for 6 h to form a sol and calcinated at 400 °C for 3 h to obtain precursor. Finially, the precursor was calcinated at 900 °C for 10 h to form LiCoO₂.

Preparation of Na₂CO₃. The commercial Na₂CO₃ (Aladdin, 99%) powder was ball-milled for 20 h to reduce particle size as the pristine reagent.

Preparation of CNTs + LCO Composite Powder. A 70 mg amount of commercial CNTs and 20 mg of LiCoO₂ nanoparticles were dissolved in 10 mL of ethanol and dispersed with the ultrasonic cell pulverizer for 3 h. Then, the mixture solution was ultrasonically heated at 70 °C to volatilize the ethanol completely.

Preparation of $Na_2CO_3/LiCoO_2$ Composite Powder. The $LiCoO_2$ nanoparticles and Na_2CO_3 powder were ball-milled for 20 h in the mass ratio of 1:9 to obtain the $Na_2CO_3/LiCoO_2$ composite powder.

Synthesis of P2 Phase Sodium Cathodes. The sodium ion battery cathodes $Na_{0.7}Mn_{0.6}Fe_{0.4}O_2$, $Na_{0.7}Fe_{0.4}Cu_{0.1}Mn_{0.5}O_2$, $Na_{0.7}Mn_{0.75}Co_{0.25}O_2$, and $Na_{0.7}CoO_2$ were synthesized by conventional solid-state synthesis route. Stoichiometric amounts of Na_2CO_3 , Mn_2O_3 , Fe_2O_3 , CuO, Co_3O_4 , and NiO powders were selectively mixed and thoroughly ground in a mortar, and then calcinated at 700 °C for 10 h in a box furnace. After cooling to room temperature, the products were transferred to an Ar-filled glovebox to avoid any moisture contamination.

Preparation of Li_{1-x}**CoO**₂ **Powder.** A 0.1 g amount of LiCoO₂ powder was directly rolled onto aluminum foil as cathode. We assembled it into a half-cell with Li metal anode, Celgard film as separator, and 1 M LiPF₆ electrolyte solution in EC/EMC (v/v = 3:7). After this was charged to 4.2 V, we disassembled the cell and rinsed the electrode with DMC to obatin Li_{1-x}CoO₂ powder.

Characterizations. The crystalline structures of materials and electrodes were investigated in a Bruker D8 Advance X-ray diffractometer (XRD) with a Cu Klpha radiation source. The morphology and elemental distribution were characterized with a scanning electron microscopy (SEM, Zeiss SUPRA-55) apparatus equipped with an energy dispersive X-ray spectrometer (EDS). The FTIR was performed on a Fourier transform infrared (FTIR) spectrometer (VERTEX 70 V). The microstructure of the material was characterized by the high-resolution transmission electron microscopy (HRTEM, JEM-100F). TEM samples were prepared using the focused ion beam (FIB, FEI Scios) method. Particularly, for CNTs, the powder was dispersed through ice bath ultrasound for 10-15 min and directly dropped on the copper mesh for the TEM test. The SC-LCO electrode was characterized by X-ray photoelectron spectra (XPS, ESCALAB 250XL). During XPS measurements, the base pressure of the sample chamber was kept below 3.0×10^{-10} mbar. The obtained emission lines were calibrated by C 1s signal at 284.6 eV. To determine the stoichiometric proportion of Na_yLi_{1-x}CoO₂, the SC-LCO eletrodes were charged to different potentials and disassembled. Then the powder obtained from the eletrodes was soaked in deionized water for 3 h and dried off under vacuum. The elemental composition was determined using ICP-AES (Horiba Jobin Yvon JY2000-2).

In Stiu X-ray Diffractometer (XRD). The in situ XRD experiments were performed in the Bruker D8 Advance diffractometer equipped with Cu K α radiation. The X-ray patterns were collected sequentially during the first charge process in a specific coin cell. The cover of the coin cell has a round detection window covered by thin polyimide film.

In Stiu Differential Electrochemical Mass Spectrometry (DEMS). In stiu DEMS (HPR-20 EGA) was used to track O_2 , CO, and CO_2 gas evolution during the first charge process. The cell consisted of a sodium anode, electrolyte (1 M NaPF₆ in ethylene carbonate (EC)/diethyl carbonate (DEC) (v/v = 1:1)), and the working positive electrode was purged continuously with Ar gas. The evolved gases were detected in the mass spectrometer in real time followed by Ar gas.

In Situ Atomic Force Microscopy (AFM). In situ AFM was carried out through a fluid cell as shown in Figure S7. To imitate the real batteries, the working electrode was composed of active material (Na₂CO₃ with or without LiCoO₂), AB, and PVDF in the same mass ratio (8:1:1) coating on the smooth aluminum substrate. The sodium metal grain was directly used as the reference and the counter electrodes. The amount of electrolyte of the in situ cell was about 0.1 mL in each test. All of the in situ AFM tests were conducted in an Arfilled glovebox with H₂O and O₂ < 0.1 ppm. A CHI660E electrochemical workstation (Chenhua Instument Co., Ltd., China) was used for LSV tests of in situ cells. The AFM images were acquired at a Bruker Multimode 8 system by using an insulating silicon nitride AFM tip in Scansyst-fluid mode, scanning at a rate of 0.5 Hz. The potential was swept from OCP to 4.8 V (vs Na/Na⁺) gradually.

Electrochemical Quartz Crystal Microbalance (EQCM). The EQCM measurements were measured with the combination of a QCM922 quartz crystal microbalance and a VersaSTAT 3 potentiostat/galvanostat. Mixtures of Na₂CO₃, AB, and PVDF with/without LiCoO₂ in the mass ratio of 8:1:1 were dripped on the gold-coated quartz crystal to compose working electrodes (reference frequency of 9 MHz). The sodium metal strings concurrently acted as counter and reference electrodes. The LSV curves were obtained from OCV to 4.3 V at the scan rate of 1 mV/s. The mass change of the electrode during the reactions can be calculated from the collected frequency of the quartz crystal with the following equation:

$$\Delta f = -\frac{2f_0^2}{A\sqrt{\rho_Q \mu_Q}} \Delta m$$

where Δf is the frequency change of the gold-coated quartz crystal electrode, ${f_0}^2$ is the resonant frequency of the quartz crystal, A is the active crystal surface, ${\rho_{\rm Q}}$ is the density of the quartz (2.648 g cm⁻³), ${\mu_{\rm Q}}$ is the shear modulus of the quartz (2.947 × 10^{11} g cm⁻¹ s⁻²), and Δm is the mass change of the electrochemical process in the working electrode.

In Situ Shell-Isolated Nanoparticle-Enhanced Raman Spectrometry (SHINES). In order to collect shell-isolated nanoparticleenhanced Raman signal (SHINER), the gold nanoparticles with a diameter of 40 nm coated with an \sim 3 nm SiO₂ shell were synthesized. Then the Au@SiO2 nanoparticles dispersed solution was dripped onto the specific cathode surface and dried under vacuum. The cathode was assembled at the bottom of the cell with the active material face upward, and both the membrance and Na foil were punched with a small hole in the center. On the top of the cell was also punched a small hole and fixed with a thin sapphire window for the laser and Raman signals' entry and collection. The Raman spectra were record using a Renishaw microscope spectrometer with a 633 nm wavelength. The laser beam power delivered to the electrode surface was 10% of the maximum 17 mW intensity. The Raman spectrum acquisition time was 300 s. The galvanostatic charge process was carried out on a Neware electrochemical workstation.

Na-CO₂ Battery Tests. The cathodes of the Na-CO₂ battery were obtained by ball milling LiCoO₂/CNTs composite powder and Nafion (mass ratio = 9:1) in ethanal for 5 h to obtain a well-dispersed slurry, which was further cast on the carbon paper with mass loading of $\sim 1.5 \text{ mg/cm}^2$. The Na-CO₂ battery was assembled with Na metal anode, glass fiber as membrane, and 0.5 M NaPF₆ electrolyte solution in tetraethylene glycol dimethyl ether (TEGDME) in an Ar-filled glovebox and run in a small glovebox with pure CO₂ atmosphere.

Na-lon Half-Cells and Full Cells. The electrode with P2-type cathode was prepared by mixing the active material, acetylene black (AB) and poly(vinylidene difluoride) (PVDF) in a mass ratio of 8:1:1 and casting onto the Al foil. The Na-ion half-cell was assembled with Na metal anode, glass fiber as membrane, and 1 M NaPF₆ electrolyte solution in EC/DEC (v/v = 1:1). The full cell was assembled with hard carbon (Kuraray) to replace the Na metal anode. The galvanostatic charge and discharge process was performed on Neware battery test systems. The linear sweep voltammetry (LSV) was tested at a scan rate of 0.1 mV s⁻¹ from 1.5 to 4.2 V.

ASSOCIATED CONTENT

Supporting Information

The Supporting Information is available free of charge at https://pubs.acs.org/doi/10.1021/acsnano.2c11029.

SEM images; XRD patterns; TEM images; first-cycle voltage profiles, currents, and particle sizes; *ex situ* SEM and SEM-EDS anaylses; LSV curves; EQCM results; *in situ* and *ex situ* XRD results; *ex situ* FTIR spectra; *ex situ* XPS spectra; DEMS results; *in situ* AFM results; ICP-AES results; cycling stability and charge—discharge profiles; performance comparison tables (PDF)

AUTHOR INFORMATION

Corresponding Authors

Luyi Yang — School of Advanced Materials, Peking University Shenzhen Graduate School, Shenzhen 518055, China; orcid.org/0000-0002-5516-9829; Email: yangly@pkusz.edu.cn

Feng Pan — School of Advanced Materials, Peking University Shenzhen Graduate School, Shenzhen 518055, China; orcid.org/0000-0002-8216-1339; Email: panfeng@pkusz.edu.cn

Authors

Weiyuan Huang — School of Advanced Materials, Peking University Shenzhen Graduate School, Shenzhen 518055, China

Jimin Qiu – School of Advanced Materials, Peking University Shenzhen Graduate School, Shenzhen 518055, China

Yuchen Ji – School of Advanced Materials, Peking University Shenzhen Graduate School, Shenzhen 518055, China

Wenguang Zhao — School of Advanced Materials, Peking University Shenzhen Graduate School, Shenzhen 518055, China

Zihang Dong — School of Environment and Energy, Peking University Shenzhen Graduate School, Shenzhen 518055, China

Kai Yang - Advanced Technology Institute, University of Surrey, Guildford, Surrey GU2 7XH, United Kingdom

Ming Yang – College of Chemistry and Environmental Engineering, Shenzhen University, Shenzhen 518060, China

Qindong Chen — School of Environment and Energy, Peking University Shenzhen Graduate School, Shenzhen 518055, China

Mingjian Zhang — School of Advanced Materials, Peking University Shenzhen Graduate School, Shenzhen 518055, China; orcid.org/0000-0002-6843-5911

Cong Lin — School of Advanced Materials, Peking University Shenzhen Graduate School, Shenzhen 518055, China; orcid.org/0000-0003-0021-5055

Kang Xu — Battery Science Branch, Sensor and Electron Devices Directorate, Power and Energy Division, U.S. Army Research Laboratory, Adelphi, Maryland 20783, United States

Complete contact information is available at: https://pubs.acs.org/10.1021/acsnano.2c11029

Author Contributions

*W.H., J.Q., and Y.J. contributed equally to this work.

Notes

The authors declare no competing financial interest.

ACKNOWLEDGMENTS

This work was supported by the National Key R&D Program of China (2020YFB0704500), the Soft Science Research Project of Guangdong Province (2017B030301013), and the Chemistry and Chemical Engineering Guangdong Laboratory (Grant No. 1922018).

REFERENCES

(1) Dinh, C. T.; Burdyny, T.; Kibria, M. G.; Seifitokaldani, A.; Gabardo, C. M.; Garcia de Arquer, F. P. G.; Kiani, A.; Edwards, J. P.; De Luna, P.; Bushuyev, O. S.; Zou, C. Q.; Quintero-Bermudez, R.; Pang, Y. J.; Sinton, D.; Sargent, E. H. CO₂ Electroreduction to

- Ethylene via Hydroxide-Mediated Copper Catalysis at an Abrupt Interface. *Science* **2018**, *360*, 783–787.
- (2) Xia, Y.; Campbell, C. T.; Roldan Cuenya, B.; Mavrikakis, M. Introduction: Advanced Materials and Methods for Catalysis and Electrocatalysis by Transition Metals. *Chem. Rev.* **2021**, *121*, 563–566.
- (3) Yang, T. H.; Ahn, J.; Shi, S.; Wang, P.; Gao, R. Q.; Qin, D. Noble-Metal Nanoframes and Their Catalytic Applications. *Chem. Rev.* 2021, 121, 796–833.
- (4) Tamirat, A. G.; Guan, X.; Liu, J.; Luo, J.; Xia, Y. Redox Mediators as Charge Agents for Changing Electrochemical Reactions. *Chem. Soc. Rev.* **2020**, *49*, 7454–7478.
- (5) Adams, J. S.; Chemburkar, A.; Priyadarshini, P.; Ricciardulli, T.; Lu, Y.; Maliekkal, V.; Sampath, A.; Winikoff, S.; Karim, A. M.; Neurock, M.; Flaherty, D. W. Solvent molecules form surface redox mediators in situ and cocatalyze O₂ reduction on Pd. *Science* **2021**, 371, 626–632.
- (6) Chen, Y.; Freunberger, S. A.; Peng, Z.; Fontaine, O.; Bruce, P. G. Charging a Li-O₂ battery using a redox mediator. *Nat. Chem.* **2013**, *5*, 489–94.
- (7) Gao, X.; Chen, Y.; Johnson, L.; Bruce, P. G. Promoting solution phase discharge in Li- O_2 batteries containing weakly solvating electrolyte solutions. *Nat. Mater.* **2016**, *15*, 882–8.
- (8) Gao, X.; Chen, Y.; Johnson, L. R.; Jovanov, Z. P.; Bruce, P. G. A rechargeable lithium—oxygen battery with dual mediators stabilizing the carbon cathode. *Nat. Energy* **2017**, *2*, 17118.
- (9) Xia, C.; Kwok, C. Y.; Nazar, L. F. A high-energy-density lithium-oxygen battery based on a reversible four-electron conversion to lithium oxide. *Science* **2018**, *361*, 777–781.
- (10) Asadi, M.; Sayahpour, B.; Abbasi, P.; Ngo, A. T.; Karis, K.; Jokisaari, J. R.; Liu, C.; Narayanan, B.; Gerard, M.; Yasaei, P.; Hu, X.; Mukherjee, A.; Lau, K. C.; Assary, R. S.; Khalili-Araghi, F.; Klie, R. F.; Curtiss, L. A.; Salehi-Khojin, A. A lithium-oxygen battery with a long cycle life in an air-like atmosphere. *Nature* **2018**, *555*, 502–506.
- (11) Qiao, Y.; Yi, J.; Wu, S.; Liu, Y.; Yang, S.; He, P.; Zhou, H. Li-CO₂ Electrochemistry: A New Strategy for CO₂ Fixation and Energy Storage. *Joule* **2017**, *1*, 359–370.
- (12) Aetukuri, N. B.; McCloskey, B. D.; Garcia, J. M.; Krupp, L. E.; Viswanathan, V.; Luntz, A. C. Solvating additives drive solution-mediated electrochemistry and enhance toroid growth in non-aqueous Li-O(2) batteries. *Nat. Chem.* **2015**, *7*, 50–6.
- (13) Pang, Q.; Kwok, C. Y.; Kundu, D.; Liang, X.; Nazar, L. F. Lightweight Metallic MgB₂ Mediates Polysulfide Redox and Promises High-Energy-Density Lithium-Sulfur Batteries. *Joule* **2019**, *3*, 136–148.
- (14) Mu, X.; Pan, H.; He, P.; Zhou, H. Li-CO₂ and Na-CO₂ Batteries: Toward Greener and Sustainable Electrical Energy Storage. *Adv. Mater.* **2019**, *32*, 1903790.
- (15) Johnson, L.; Li, C.; Liu, Z.; Chen, Y.; Freunberger, S. A.; Ashok, P. C.; Praveen, B. B.; Dholakia, K.; Tarascon, J. M.; Bruce, P. G. The role of LiO₂ solubility in O₂ reduction in aprotic solvents and its consequences for Li-O₂ batteries. *Nat. Chem.* **2014**, *6*, 1091–9.
- (16) Khurram, A.; He, M.; Gallant, B. M. Tailoring the Discharge Reaction in Li-CO₂ Batteries through Incorporation of CO₂ Capture Chemistry. *Joule* **2018**, *2*, 2649–2666.
- (17) Liu, Y.; Cai, J.; Zhou, J.; Zang, Y.; Zheng, X.; Zhu, Z.; Liu, B.; Wang, G.; Qian, Y. Tailoring The Adsorption Behavior Of Superoxide Intermediates On Nickel Carbide Enables High-Rate Li-O₂ Batteries. eScience 2022, 2, 389–399.
- (18) Li, X.; Wang, H.; Chen, Z.; Xu, H. S.; Yu, W.; Liu, C.; Wang, X.; Zhang, K.; Xie, K.; Loh, K. P. Covalent-Organic-Framework-Based Li-CO₂ Batteries. *Adv. Mater.* **2019**, *31*, 1905879.
- (19) Qiao, Y.; Jiang, K.; Deng, H.; Zhou, H. A high-energy-density and long-life lithium-ion battery via reversible oxide—peroxide conversion. *Nat. Catal.* **2019**, *2*, 1035–1044.
- (20) Zhang, L.; Dambournet, D.; Iadecola, A.; Batuk, D.; Borkiewicz, O. J.; Wiaderek, K. M.; Salager, E.; Shao, M.; Chen, G.; Tarascon, J.-M. Origin Of The High Capacity Manganese-Based Oxyfluoride

- Electrodes For Rechargeable Batteries. *Chem. Mater.* **2018**, 30, 5362–5372.
- (21) Jung, S.-K; Kim, H.; Cho, M. G.; Cho, S.-P.; Lee, B.; Kim, H.; Park, Y.-U.; Hong, J.; Park, K.-Y.; Yoon, G.; Seong, M. W.; Cho, Y.; Oh, H. M.; Kim, H.; Gwon, H.; Hwang, I.; Hyeon, T.; Yoon, W.-S.; Kang, K. Lithium-Free Transition Metal Monoxides For Positive Electrodes In Lithium-Ion Batteries. *Nat. Energy* **2017**, *2*, 16208.
- (22) Hwang, J. Y.; Myung, S. T.; Sun, Y. K. Sodium-ion batteries: present and future. *Chem. Soc. Rev.* 2017, 46, 3529–3614.
- (23) Song, S.; Li, Y.; Yang, K.; Chen, Z.; Liu, J.; Qi, R.; Li, Z.; Zuo, C.; Zhao, W.; Yang, N.; Zhang, M.; Pan, F. The interplay between multiple doping elements in high-voltage LiCoO₂. *J. Mater. Chem. A* **2021**, *9*, 5702–5710.
- (24) Taguchi, N.; Akita, T.; Tatsumi, K.; Sakaebe, H. Characterization of MgO-coated-LiCoO2 particles by analytical transmission electron microscopy. *J. Power Sources* **2016**, 328, 161–166.
- (25) Yang, Q.; Huang, J.; Li, Y.; Wang, Y.; Qiu, J.; Zhang, J.; Yu, H.; Yu, X.; Li, H.; Chen, L. Surface-protected LiCoO₂ with ultrathin solid oxide electrolyte film for high-voltage lithium ion batteries and lithium polymer batteries. *J. Power Sources* **2018**, 388, 65–70.
- (26) Yang, Z.; Ong, P. V.; He, Y.; Wang, L.; Bowden, M. E.; Xu, W.; Droubay, T. C.; Wang, C.; Sushko, P. V.; Du, Y. Direct Visualization of Li Dendrite Effect on LiCoO₂ Cathode by In Situ TEM. *Small* **2018**, *14*, 1803108.
- (27) Hwang, S.; Lee, Y.; Jo, E.; Chung, K. Y.; Choi, W.; Kim, S. M.; Chang, W. Investigation of Thermal Stability of P2-NaxCoO₂ Cathode Materials for Sodium Ion Batteries Using Real-Time Electron Microscopy. *ACS Appl. Mater. Interfaces* **2017**, *9*, 18883–18888.
- (28) Mattila, N.; Karttunen, A. J. Lattice thermal conductivity of NaCoO₂ and LiCoO₂ intercalation materials studied by hybrid density functional theory. *Mater. Res. Express* **2020**, *7*, 075502.
- (29) Liu, Q.; Tang, Y.; Sun, H.; Yang, T.; Sun, Y.; Du, C.; Jia, P.; Ye, H.; Chen, J.; Peng, Q.; Shen, T.; Zhang, L.; Huang, J. In Situ Electrochemical Study of Na-O₂/CO₂ Batteries in an Environmental Transmission Electron Microscope. *ACS Nano* **2020**, *14*, 13232–13245.
- (30) Orvananos, B.; Malik, R.; Yu, H.-C.; Abdellahi, A.; Grey, C. P.; Ceder, G.; Thornton, K. Architecture Dependence on the Dynamics of Nano-LiFePO₄ Electrodes. *Electrochimi. Acta* **2014**, *137*, 245–257.
- (31) Ren, W.; Chen, H.; Qiao, R.; Lin, Y.; Pan, F. In situ probing of interfacial kinetics for studying the electrochemical properties of active nano/micro-particles and the state of Li-ion batteries. *J. Mater. Chem. A* **2017**, *5*, 22598–22606.
- (32) Lee, K. T.; Kan, W. H.; Nazar, L. F. Proof of Intercrystallite Ionic Transport in LiMPO₄ Electrodes (M = Fe, Mn). *J. Am. Chem. Soc.* **2009**, *131*, 6044–6045.